Department of Physics and Astronomy
University of Heidelberg

Bachelor Thesis in Physics
submitted by

Christoph Rieß

born in Kassel (Germany)

2017

Measurement of the CP asymmetry in the Decay $B^+ \to J/\psi \, K^{*+}$

This Bachelor Thesis has been carried out by Christoph Rieß at
Physikalisches Institut in Heidelberg
under the supervision of
Prof. Stephanie Hansmann-Menzemer

Abstract

In this thesis the measurement of the CP asymmetry in the decay $B^+ \to J/\psi\, K^{*+}$ is presented. The data used was recorded at the LHCb experiment in proton-proton collisions in the year 2012 at a center-of-mass energy of $\sqrt{s} = 8\,\mathrm{TeV}$ corresponding to an integrated luminosity of $\mathcal{L} \approx 2\,\mathrm{fb}^{-1}$. For this analysis the J/ψ is reconstructed from two muons, whereas the K^{*+} is reconstructed as $K_\mathrm{S}^0 \pi^+$ with $K_\mathrm{S}^0 \to \pi^+ \pi^-$. The mass spectrum of the B^+ and K^{*+} candidates are used to obtain the signal yield and the following CP asymmetry is determined:

$$A^{CP}(B^+ \to J/\psi\, K^{*+}) = (+0.40 \pm 0.60(\text{stat.}) \pm 0.48(\text{syst.}))\%.$$

This result is consistent with a former measurement performed by the BABAR collaboration but has smaller uncertainties.

Zusammenfassung

In dieser Arbeit wird die Messung der CP-Asymmetrie im Zerfall $B^+ \to J/\psi\, K^{*+}$ vorgestellt. Die genutzten Daten wurden vom LHCb Experiment im Jahr 2012 bei einer Schwerpunktsenergie von $\sqrt{s} = 8\,\mathrm{TeV}$ aufgenommen. Dies entspricht einer integrierten Luminosität von $\mathcal{L} \approx 2\,\mathrm{fb}^{-1}$. Für diese Analyse wurden Zerfälle des J/ψ in zwei Muonen verwendet, wohingegen K^{*+} als $K_\mathrm{S}^0 \pi^+$ mit $K_\mathrm{S}^0 \to \pi^+ \pi^-$ rekonstruiert wurde. Die Anzahl der Signalereignisse wurde aus den Massenspektren der B^+ und K^{*+} Kandidaten bestimmt und daraus folgende CP-Asymmetrie berechnet:

$$A^{CP}(B^+ \to J/\psi\, K^{*+}) = (+0.40 \pm 0.60(\text{stat.}) \pm 0.48(\text{syst.}))\%.$$

Dieses Ergebnis ist konsistent mit einer früheren Messung der BABAR-Kollaboration, hat jedoch kleinere Unsicherheiten.

Contents

1 Introduction

Particle physics deals with one of nature's most fundamental properties: The constituents of matter, called *elementary particles*, and their interactions, the *forces*. While looking for a correct description of particles and their interactions, the so-called Standard Model (SM) [1] of particle physics has been established. With the discovery of the Higgs Boson [2] the last missing piece of the SM has been observed. Predictions of the Standard Model have been tested and confirmed over the last decades and were found to be consistent with all results from laboratory experiments. Nevertheless, the SM cannot be the final theory as open questions remain. Neither dark energy and dark matter, which are thought to make up over 90% of the Universe, nor gravitation are part of the Standard Model. While the SM predicts neutrinos to be massless, experimental results have proven neutrino oscillations for which neutrinos have to be massive. Additionally, the asymmetry between matter and antimatter observed in the universe cannot be explained by the SM. The SM includes so-called CP violation which leads to a different behavior between particles and antiparticles and could therefore in principle account for those asymmetries. However, it is too small to make up for the asymmetry observed.

The LHC (Large Hadron Collider) at CERN was build to find new particles and answers to abovementioned questions (so-called *physics beyond the Standard Model*). It is a proton-proton collider and the world's most powerful particle accelerator. The four large experiments at the LHC are CMS, ATLAS, ALICE and LHCb. The LHCb experiment is dedicated to hadrons containing a bottom or charm quark. These hadrons are of special interest in the search for CP violation since the heavy b quark facilitates a precise theoretical description. Any measurement of a significant deviation from theoretical predictions would be a hint for physics beyond the Standard Model. Since no deviations have been found so far, the effect of physics beyond the Standard Model has to be small. The B^+, whose decay $B^+ \to J/\psi \, K^{*+}$ is studied in this thesis, is an example of these bottom hadrons. To determine the CP asymmetry of this decay one first measures the raw CP asymmetry

$$A_{raw}^{CP} = \frac{N(B^- \to J/\psi \, K^{*-}) - N(B^+ \to J/\psi \, K^{*+})}{N(B^- \to J/\psi \, K^{*-}) + N(B^+ \to J/\psi \, K^{*+})}$$

where N is the number of events, which has then to be corrected for further sources of asymmetries, such as a possible production asymmetry and other effects. So far, the CP asymmetry in this decay was measured to be $A^{CP} = (-4.8 \pm 2.9(\text{stat.}) \pm 1.6(\text{syst.}))\%$ by the BABAR collaboration [3]. With a larger sample of B mesons from the LHCb better statistics can be achieved. The dataset used in this thesis was recorder with the LHCb detector in the year 2012 at a center-of-mass energy of $\sqrt{s} = 8\,\text{TeV}$ corresponding to an integrated luminosity of $\mathcal{L} \approx 2\,\text{fb}^{-1}$.

The thesis is structured in the following way: Section 2 gives an introduction to the theory of particle physics and the Standard Model followed by an overview about the experimental setup in Section 3. Provided with all theoretical and experimental knowledge needed, a summary of the analysis and the used variables can be found in Section 4. The data selection including a multivariate analysis is explained in Section 5. The determination of the CP asymmetry is performed in Section 6. After a discussion of systemic uncertainties in Section 7, the final result is presented in Section 8.

2 Theoretical overview

In this section the basic concepts of particle physics are introduced. First, the Standard Model (SM) of particle phyiscs is presented with a focus on flavor physics and CP violation. In the last part of the section the decay which is investigated in this thesis is explained in more detail. A full introduction to the SM can be found in [1].

2.1 The Standard Model

The Standard Model of particle physics is a quantum field theory and a comprehensive description of elementary particles and their interactions (excluding gravitation). The SM includes so-called fermions which make up all visible mat-

Figure 2.1: Elementary particles of the Standard Model of particle physics. Quarks/leptons in the same column are said to be in the same generation/family. Figure taken from [4].

ter and the mediator particles of their interactions called bosons (see Fig. 2.1). Fermions carry spin $\frac{1}{2}$ while bosons have spin 1. There exists an antiparticle for each of the 12 fermions with the same mass and inverted quantum numbers. Fermions can be further divided in 6 quarks (up, down, charm, strange, top, bottom) and 6 leptons (electron, electron neutrino, muon, muon neutrino, tau, tau neutrino). One can subclassify the quarks and leptons in three families. Quark families consist of an up-type quark with electric charge $\frac{2}{3}$ and a down-type quark of charge $-\frac{1}{3}$. The apparent matter consists of the light[1] first quark generation and electrons. The three lepton families are each made of a lepton with electric charge -1 and a neutral neutrino. The type of a particle is called *flavor*.

One distinguishes between three fundamental forces: The strong interaction, the weak interaction and the electromagnetic interaction. Each is realized by the exchange of a gauge boson which only couples to a specific quantum number of the particle.

Quarks carry color charge, which is the charge of the **strong interaction**. The color charges are conventionally called red, green and blue. Quarks form composite objects (called hadrons), either consisting of a quark and an anti-quark (mesons) or three (anti-)quarks ((anti-)baryons). Recently, the existence of particles consisting of four or five quarks (tetra- and pentaquarks, respectively, see [5]) has been established. All these composite particles are colorless[2]. In fact, free colored particles have never been observed. The mediating gauge bosons are called gluons and carry a combination of a color and an anti-color. Thus, only quarks and the massless gluons participate in the strong interaction. The potential energy between two quarks rises with their distance which leads to the fact that the creation of a quark-anti-quark-pair is energetically favored. This leads to the so-called *confinement*. The strong interaction is also responsible for an attractive force between neutrons and protons in atomic nuclei. The underlying quantum field theory is *Quantum Chromodynamics* (QCD).

As the name suggests the **electromagnetic interaction** couples to all electrically charged particles. The interacting particle is the massless photon (γ). The theory describing the electromagnetic interaction is *Quantum Electrodynamics* (QED).

The mediator particles of the **weak interaction** are the massive $W^{\pm}$ and Z bosons. Due to the mass of its gauge bosons the weak interaction is suppressed in comparison to the strong or electromagnetic interaction. Only in the weak interaction flavor change is possible which makes it especially important for the

---

[1] u and d quark have a mass of a few MeV while quarks of the other two generations have masses up to $173 \, \text{GeV}$ (top quark).

[2] In a colorless particle the net color charge is the same for all three colors.

Interaction	Boson		Spin	Mass[GeV]
Strong	Gluon	g	1	0
Electromagnetism	Photon	γ	1	0
Weak	W boson	$W^{\pm}$	1	80.4
	Z boson	Z	1	91.2

Table 1: The three forces of the SM. Natural units ($\hbar=c=1$) are used here as well as in the rest of this thesis.

decay studied in this thesis.

Albeit not of big importance here it should be mentioned that electromagnetic and weak interaction can be combined in the so-called electroweak interaction, whereas a unification of all three forces (Grand Unified Theory) has not been found yet.

The final element of the SM is the Higgs boson which was also the last to be observed [2]. It is a neutral scalar. The excitation of the Higgs field is used to explain the masses of the massive fundamental SM particles and the $W^{\pm}$ and Z.

2.2   Flavor physics

Particles can change their flavor via the weak interaction. More precisely, quarks transform from an up-type to a down-type quark or vice versa. This is described by the Cabibbo-Kobayashi-Maskawa (CKM) mechanism given by the unitary matrix V_{CKM}

$$\begin{pmatrix} d' \\ s' \\ b' \end{pmatrix} = \begin{pmatrix} V_{ud} & V_{us} & V_{ub} \\ V_{cd} & V_{cs} & V_{cb} \\ V_{td} & V_{ts} & V_{tb} \end{pmatrix} \begin{pmatrix} d \\ s \\ b \end{pmatrix} \tag{2.1}$$

where (d', s', b') are the eigenstates of the weak interaction and (d, s, b) the mass eigenstates. The probability for such a transition between the quarks i and j is proportional to $|V_{ij}|^2$. Due to its unitarity the CKM matrix has four free parameters and can be described by three rotation angles and a complex phase δ:

$$\begin{pmatrix} V_{ud} & V_{us} & V_{ub} \\ V_{cd} & V_{cs} & V_{cb} \\ V_{td} & V_{ts} & V_{tb} \end{pmatrix} = \begin{pmatrix} 1 & 0 & 0 \\ 1 & c_{23} & s_{23} \\ 0 & -s_{23} & Vc_{23} \end{pmatrix} \times \begin{pmatrix} c_{13} & 0 & s_{13}e^{-i\delta} \\ 0 & 1 & 0 \\ -s_{13}e^{i\delta} & 0 & c_{13} \end{pmatrix} \times \begin{pmatrix} c_{12} & s_{12} & 0 \\ -s_{12} & c_{12} & 0 \\ 0 & 0 & 1 \end{pmatrix} \tag{2.2}$$
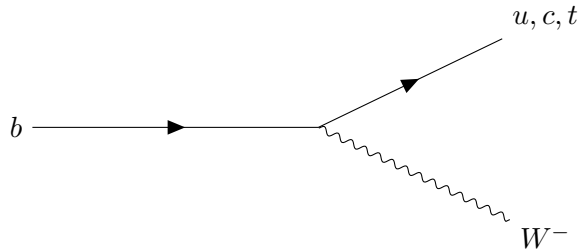
Figure 2.2: Feynman diagram of a flavor changing charged current. Only the flavor changing part of the process is shown.

where $s_{ij} = \sin\theta_{ij}$ and $c_{ij} = \cos\theta_{ij}$. The absolute values of the matrix elements are given by [1]

$$\begin{pmatrix} |V_{ud}| & |V_{us}| & |V_{ub}| \\ |V_{cd}| & |V_{cs}| & |V_{cb}| \\ |V_{td}| & |V_{ts}| & |V_{tb}| \end{pmatrix} \approx \begin{pmatrix} 0.974 & 0.225 & 0.004 \\ 0.225 & 0,973 & 0.041 \\ 0.009 & 0.040 & 0.999 \end{pmatrix} \tag{2.3}$$

It is apparent that transitions within the same generation, given by the diagonal elements, are favored. Other transitions are possible but more unlikely, they are said to be Cabibbo suppressed.

In lowest order Feynman diagrams (tree level) direct decays from an up-type to a down-type quark are realized by radiation of a $W^{\pm}$ (see Fig. 2.2). These interactions are called *flavor changing charged currents* since the $W^{\pm}$ has an electric charge.

In higher order Feynman diagrams other decays, involving more than one gauge boson, are possible as well as *flavor changing neutral currents* where the net charge does not change. These higher order decay modes are Cabibbo suppressed.

2.3 *CP* violation

As a quantum field theory the SM is invariant under combined CPT[3] - transformation but not under individual transformations of C, P and T. The Lagrangian of the weak interaction is not invariant under CP transformation and thus weak interactions violate the combined CP symmetry [6]. The observation of said violation was first made in the neutral kaon system.

One distinguishes between three different types of CP violation.

CP violation in mixing happens in neutral meson systems in an oscillation (e.g. $B^0\bar{B}^0$ oscillation) where the probability $\mathcal{P}(B^0 \to \bar{B}^0)$ is different from the probability $\mathcal{P}(\bar{B}^0 \to B^0)$.

---

[3]C stands for charge conjugation, P for parity (spatial inversion) and T for time reversal

Direct CP violation or CP violation in decay comes from the difference between decay probabilities of CP-conjugate processes: $\mathcal{P}(B \to f) \neq \mathcal{P}(\bar{B} \to \bar{f})$ with some final state f.

The third type is an **interference** between the direct decay and a decay via mixing as it happens in neutral meson systems where particle and antiparticle can decay into the same final state.

For each of these types to happen in a decay there must be an interference of at least two different amplitudes describing the transition from the initial to the final state. CP violation then enters because the so-called *weak phase*[4] ϕ_W of one of the amplitudes changes sign under CP transformation whereas the *strong phase* ϕ_S does not. With the amplitudes A_1 and A_2 for the processes one gets:

$$A_1 = \mathcal{A}_1, A_2 = \mathcal{A}_2 e^{i\phi_W} e^{i\phi_S} \tag{2.4}$$

$$\to |A_1 + A_2|^2 - |\bar{A}_1 + \bar{A}_2|^2 = \mathcal{A}_1^2 + \mathcal{A}_2^2 + 2\mathcal{A}_1 \cdot \mathcal{A}_2 e^{i\phi_W} e^{i\phi_S} \tag{2.5}$$

$$- \mathcal{A}_1^2 + \mathcal{A}_2^2 - 2\mathcal{A}_1 \cdot \mathcal{A}_2 e^{-i\phi_W} e^{i\phi_S} \tag{2.6}$$

$$= -4\mathcal{A}_1 \cdot \mathcal{A}_2 \sin\phi_W \sin\phi_S \tag{2.7}$$

The weak phase appears in the CKM matrix whereas the strong phase is part of the CP conserving strong interaction. Note that both a non-zero weak phase and a non-zero strong phase are needed to establish non-zero CP violation

2.4 B meson physics

The B meson system is of special interest in the search for CP violation. B mesons are made of a heavy b quark as well as a lighter quark from the first two generations. In calculations, the light quark can be seen as a *spectator* quark. This facilitates the use of approximations and symmetries in theoretical calculations of the B meson system that are not valid for mesons with lower masses.

There is a large number of B mesons produced at the LHC. Together with their many decay modes and other properties like their long lifetimes (leading to a spatially distinguishable decay point) this sets up good conditions for studies of B mesons.

The heavy b quark and the fact that the CKM favored transition b→t is kinematically forbidden in tree level decays also leads to a large amount of higher order diagrams in the B meson system[5].

---

[4]More precisely: phase difference.

[5]The amplitude for weak interactions is proportional to the corresponding element of the CKM matrix. $|V_{tb}|$ is almost 1 and since the coupling strength for a virtual process is proportional to the mass of a quark, virtual top quarks dominate. This leads to higher order diagrams.

2.5 Decay $B^+ \to J/\psi\, K^{*+}$
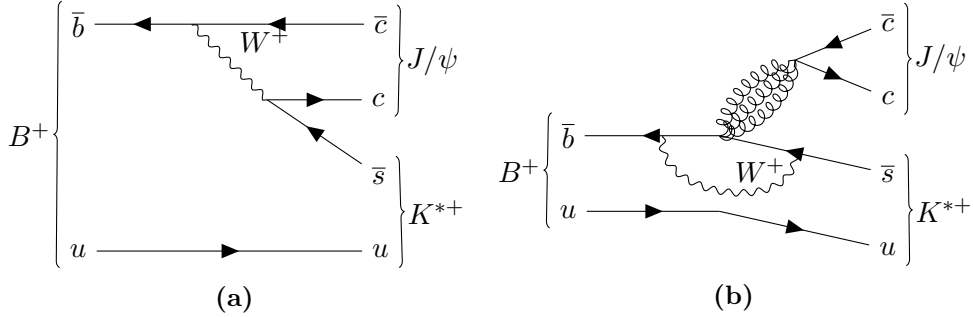
Figure 2.3: The tree level diagram (a) for $B^+ \to J/\psi\, K^{*+}$, where the $\bar{b}$ transforms into $\bar{c}$ by radiating W^+ which decays into c and $\bar{s}$, and the penguin diagram (b) for the same process are shown including a quark loop.

In this thesis the decay $B^+ \to J/\psi\, K^{*+}$ is studied[6] in view of the search for direct CP violation. The channel of J/ψ decaying into two muons is used, whereas the K^{*+} is reconstructed as $K^0_S \pi^+$ with $K^0_S \to \pi^+\pi^-$. The J/ψ and K^{*+} have such short lifetimes that it is impossible to spatially resolve their traveled distance. Therefore the muons, K^0_S and the π^+ seem to emerge from the same vertex.

In Fig. 2.3 the decay is shown on tree level and a possible penguin diagram which is much less likely to happen. The expected CP violation caused by the interference of these diagrams is therefore small (see Equ. 2.7).

To get the CP asymmetry given by

$$A^{CP} = \frac{\mathcal{B}(B^- \to J/\psi\, K^{*-}) - \mathcal{B}(B^+ \to J/\psi\, K^{*+})}{\mathcal{B}(B^- \to J/\psi\, K^{*-}) + \mathcal{B}(B^+ \to J/\psi\, K^{*+})} \qquad (2.8)$$

one first measures the raw CP asymmetry

$$A^{CP}_{raw} = \frac{N(B^- \to J/\psi\, K^{*-}) - N(B^+ \to J/\psi\, K^{*+})}{N(B^- \to J/\psi\, K^{*-}) + N(B^+ \to J/\psi\, K^{*+})} \qquad (2.9)$$

where N is the number of observed events. To calculate A^{CP} one has to take into account asymmetries in the production of B^+ and B^- as well as differences in the interaction with matter of the final state particles.

So far, the only measurement of this CP asymmetry resulted in $A^{CP} = -0.048 \pm 0.029 \pm 0.016$ [3] where the first uncertainty is statistical and the second systematic.

---

[6]Charge conjugation is implied, if not otherwise stated.

3 Experimental Setup

The first part of this section gives a general overview about the LHC (Large Hadron Collider) at CERN[7] before coming to a more detailed description of the LHCb (Large Hadron Collider beauty) detector where the data for this thesis was taken in the year 2012. More information about LHCb can be found in [7].

3.1 LHC

The LHC at CERN in Geneva, Switzerland, is a circular proton-proton collider placed in an tunnel of 27 km circumference underneath the Swiss-French border (see Fig. 3.1). The maximum center of mass energy is $\sqrt{s} = 14\,\text{TeV}$ which is to be archieved gradually. In 2012 the energy was $\sqrt{s} = 8\,\text{TeV}$. The LHC currently holds the world record with an energy of $\sqrt{s} = 13\,\text{TeV}$. The two proton beams, running in opposite directions, consist of 2808 bunches with 10^{11} protons each. They meet at the 4 collision points with a rate of 40 MHz. There are four large experiments operating, one at each collision point. Besides the abovely mentioned LHCb experiment these are ATLAS (A Toroidal LHC Apparatus [9]), CMS (Compact Muon Solenoid [10]) and ALICE (A Large Ion Collider Experiment [11]). While ATLAS and CMS are seacrhing for high mass resonances (like the found Higgs boson, [2]) and other signatures of physics
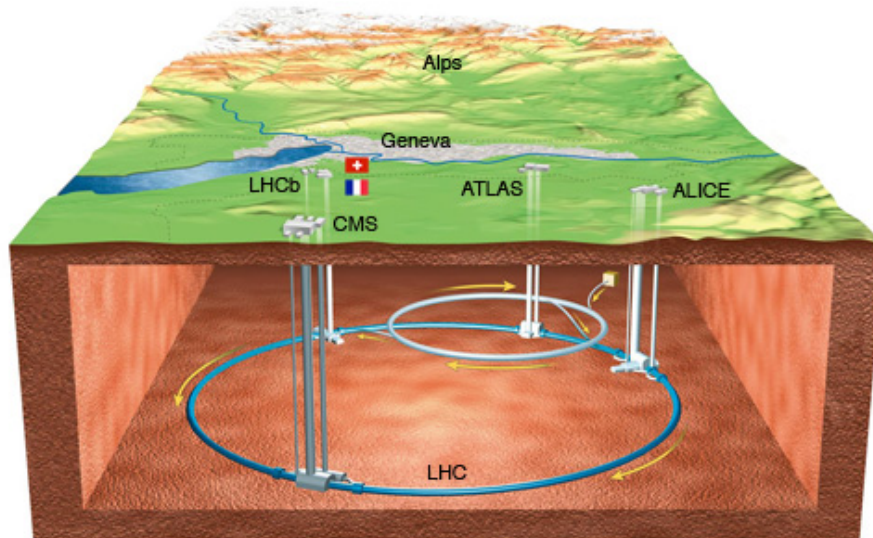
Figure 3.1: Illustration of the geographical location of the LHC and the four large experiments. Taken from [8].

---

[7]Organisation Européen pour la Recherche Nucleáire, The European Organization for Nuclear Research

beyond the SM, the ALICE detector is dedicated to the analysis of heavy ion collisions and the investigation of the quark gluon plasma.

The LHCb detector was build to study b and c hadrons. Its aim is a more precise measurement of loop induced processes like CP violation and rare decays. It therefore enables indirect searches for new physics.

3.2   The LHCb detector

The LHCb detector is specialized on detecting bottom[8] and charm hadrons, which are produced in pairs and are highly boosted in the directions of the beams. Therefore, LHCb is a dedicated forward spectrometer. The detector covers a region from 10 to 250 mrad in the y-z-plane and from 10 to 300 mrad in the x-z-plane. LHCb has a unique forward coverage compared to the other experiments at CERN. Fig. 3.2 shows a side view of the 5600 t, 21 m long, 10 m high and 13 m wide detector.

3.2.1   Magnet

The LHCb magnet consists of two identical saddle-shaped, water cooled aluminum coils of 27 t. They are placed mirror-symmetrically above and below
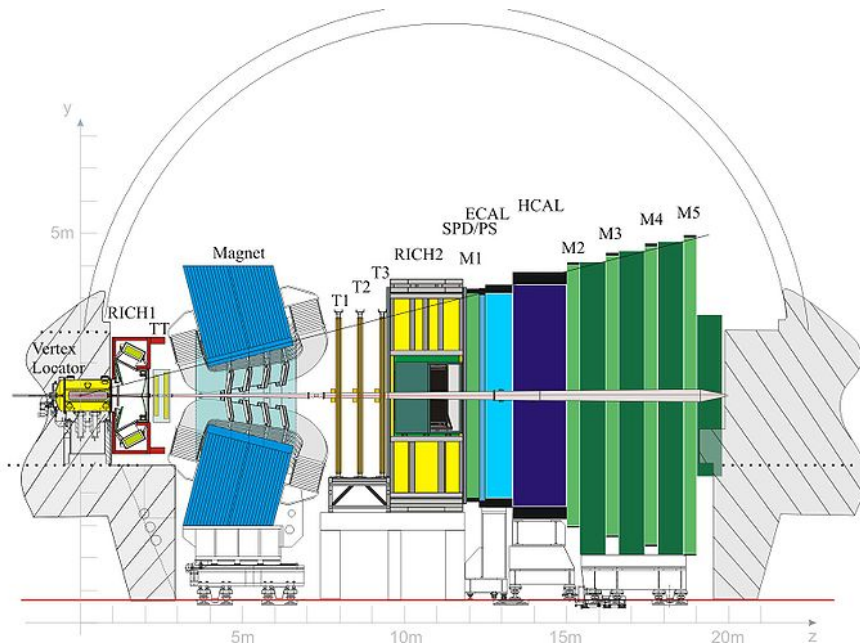
Figure 3.2: Sideview of the LHCb detector. The abbreviation of the subdetectors are explained in the following subsections. Figure taken from [7].

---

[8]also called beauty, therefore the name of the detector

the beam pipe. Its magnetic field strength, integrated along the z-axis, is approximately 4 Tm for particles passing the entire field. The magnet is bending trajectories of charged particles perpendicular to the field lines. By measuring the kink between the track before and after the magnet, it is then possible to determine the particle's momentum. It is possible to periodically switch the polarity of the magnet which allows to correct for possible detector asymmetries.

3.2.2   Tracking system

The tracking system can be divided in several subsystems: The Vertex Locator (VELO) and the Trigger Tracker (TT) before the magnet and the three tracking stations (T1-T3) after the magnet. Their main task is a precise determination of position and momentum of charged particles. The later one is done by measuring the change in the slopes caused by the magnetic field.

Vertex Locator The vertex locator (VELO) is placed directly around the interaction point and measures trajectories of charged particles. Thereby, it identifies the primary vertices (PV) and reconstructs possible displaced secondary vertices. It therefore enables a determination of the decay length and thus the decay time as well as a distinction between background particles created at the interaction point and daughter particles originating from the secondary vertex. The VELO consists of 21 pairs of silicon modules placed concentrically along the beam axis measuring the radial and azimuthal position in the x-y-plane. Their spatial resolution as about 4 μm [12].

Silicon Tracker The Tracker Turicensis or Trigger Tracker (TT) is located between VELO and magnet. It consists of two stations separated by 27 cm. Each station is further split into two silicon microstrip detector layers. They have a strip pitch of about 200 μm, leading to a resolution of 50 μm. In the first and last layer the strips are arranged vertically, in the two middle layers they are tilted by $\pm 5°$ in the x-y-plane to allow for spacial resolution in y-direction as well (see Fig. 3.3).
 The inner region of the tracking stations T1-T3 (Inner Tracker, IT) behind the magnet, where the particle flux is too high for the straw tube technology used for the Outer Tracker, is also covered with the silicon microstrip technology. Each of the three tracking stations consists of four detector layers arranged in the same way as the TT. Since the technoplogy is similar as in the TT, the measurement resolution is approximately the same.

Outer Tracker The outer part of the tracking stations is covered by straw tube detectors. They consist of 2.4 m long parallel thin straw tubes with an inner diameter of 4.9 mm. These tubes are filled with an Argon (70%) and CO_2 (30%) mixture which reduces the drift time of ionized particles to the anode wire
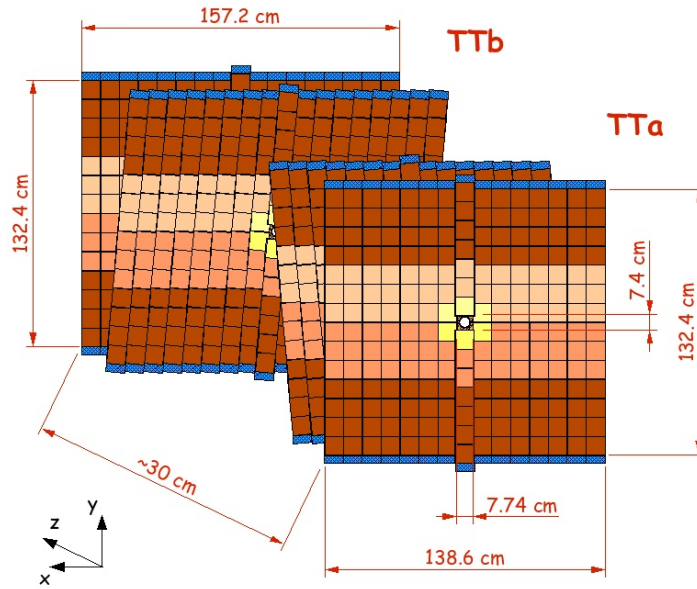
Figure 3.3: Layout of the Trigger Tracker. Taken from [13].
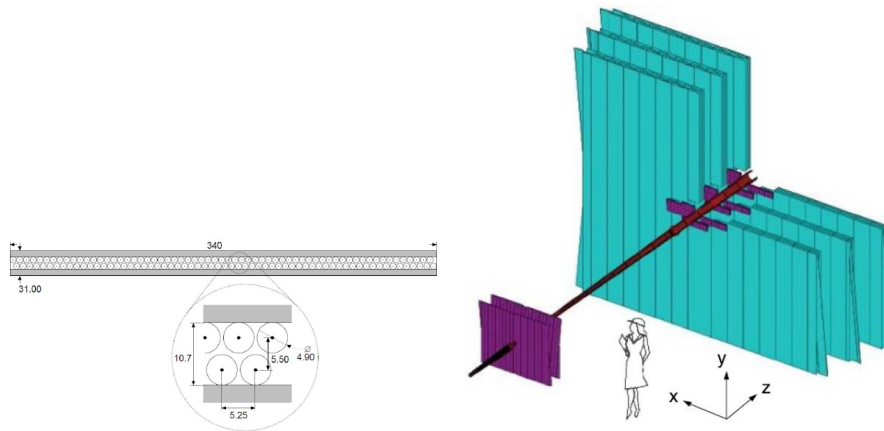
Figure 3.4: Left: Cross section of a layer consisting of two monolayers of straw tubes. Right: Layout of the tracking stations and TT (TT and IT in purple, OT in cyan). Figures taken from [7].

to below 50 ns. The drift time is then used to determine the position where a charged particle transverses the detector. A spatial resolution of about 200 µm is achieved. The tubes are put into two layers (monolayers). Each T station is made up of 4 double-layers which are again arranged in the same way as TT and IT. A schematic view of the tracking stations is shown in Fig. 3.4.

Track Reconstruction Measurements from all the previously introduced detectors are used to reconstruct the trajectories of charged particles. In this analysis long tracks, which require hits in both VELO and tracking stations (and possibly in TT), as well as downstream tracks, where the track only contains hits in the tracking stations and TT, are used.

3.2.3   Particle identification

After all information about position, direction and momentum has been collected, the final state particle needs to be identified. By using information from the particle identifications (PID) system a mass hypothesis is then established. The PID system consists of: Two Ring Imaging Cherenkov (RICH) detectors, the electromagnetic and hadronic calorimeters (ECAL and HCAL) as well as the muon chambers (M1-M5). For every possible particle hypothesis a likelihood is calculated from the PID data. Since charged pions are the most abundant particles at the LHC, the likelihoods are divided by the pion hypothesis. The logarithm of this ratio is taken: $DLL_{X\pi} = log\mathcal{L}_X - log\mathcal{L}_\pi$. In the following, said subsystems of the PID are introduced.

RICH The RICH detectors use the effect of Cherenkov radiation to distinguish between charged particles with different masses, mainly pions and kaons, which are produced in large amounts in proton-proton collisions. This radiation is emitted by a charged particle traversing a dielectric medium with refraction index n with a velocity v larger than the speed of light ($c' = \frac{c}{n}$) in that medium. Together with the momentum p measured by the tracking system the emission angle of the Cherenkov photons θ=arccos($\frac{c}{nc}$) can be used to determine the velocity and therefore the mass of the particle (see Fig. 3.5). Since for high momenta the difference in Cherenkov angles decreases, two RICH detectors with different momentum coverage are used in LHCb.
 RICH 1 is located upstream of the magnet and covers the window of 2-40 GeV in the full geometric region of LHCb. It is filled with silica aerogol (n=1.03) and gaseous C_4F_{10} (n=1.0014). RICH2 is placed downstream of the magnet after the T stations, covering the momentum region of 1-100 GeV in a smaller geometric acceptance. This is justified by the higher momentum and therefore smaller deflection caused by the magnet. RICH2 is filled with gaseous CF_4.

Calorimeter Two calorimeters are used in LHCb: An electromagnetic (ECAL) and a hadronic calorimeter (HCAL). Each calorimeter is split into many cells of scintillating material. The same principle is used in both of them: The interaction of traversing particles with the calorimeter material leads to particle showers. The hereby in the active area of the calorimeter produced light is then converted into a voltage by photomultiplier tubes (PMT). This voltage contains information about the amount of energy disposed in the corresponding cell.
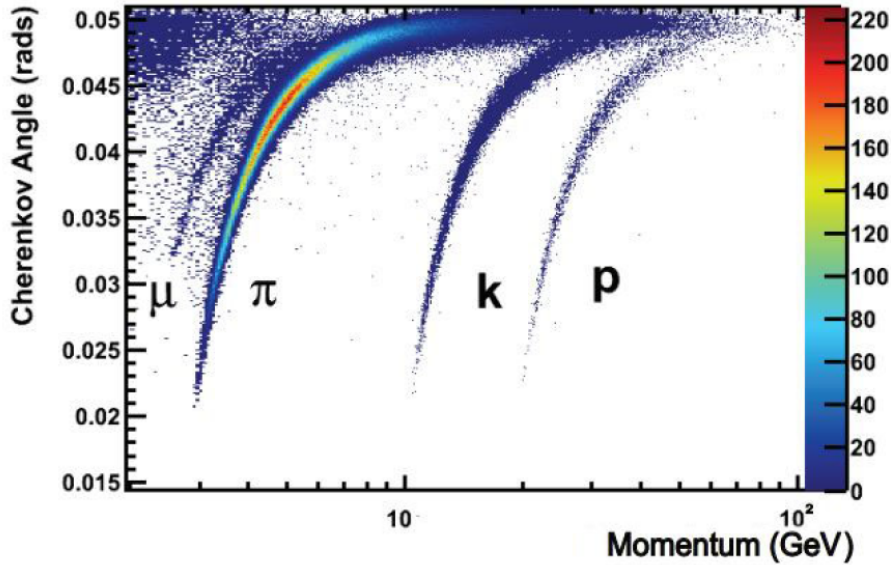
Figure 3.5: Reconstructed Cherenkov angle θ as functio of particle momentum p in RICH1. Taken from [14].

In front of the calorimeters a Scintillating Pad Detector (SPD) is placed. It is made up of a small scintillating plate which only triggers a signal if a charged particle travels through it. Background from neutral particles is therefore reduced.

Downstream of the SPD a PreShowher detector (PS) consisting of two layers of scintillating pads is placed. Between the two layers there is a 15 mm lead wall (2.5 electron radiation length) to create electromagnetic showers. Since the interaction length of hadrons is much higher, the PS is an effective tool to distinguish between electrons and hadrons, e.g. charged pions.

The ECAL is composed of alternating layers of active scintillator material and absorption layers to produce showers. The whole calorimeter corresponds to 25 radiation lengths. Hence, electrons and photons deposit all their energy in the ECAL. The energy resolution is $\sigma_E/E = \frac{10\%}{\sqrt{E}} \oplus 1\%$ for energy E in GeV. The first term comes from statistical fluctuations whereas the second term describes systematic effects.

The HCAL works similar to the ECAL, but has a thickness of 5.6 hadronic interactions lengths due to spatial limitations. Its energy resolution is worse because of higher fluctuations of the deposed energy and the lower thickness: $\sigma_E/E = \frac{(69\pm5)\%}{\sqrt{E}} \oplus (9\pm2)\%$ (E in GeV).

Muon chambers Since they do not interact hadronically, muons can easily pass through the calorimeter system described above. Since they are produced in

many interesting B decays, LHCb uses an effective system for their identification. The muon system is built up from 5 muon stations (M1-M5). All stations use Multiwire Proportional Chambers (MWPC). M1 is located upstream of the calorimeters and is used for the first trigger stage L0 (see Sec. 3.2.4). It uses additionally an GEM (gas electron multiplier) in the high-flux region around the beampipe. The other four muon stations are placed downstream of the calorimeters, separated by 80 cm thick iron absorbers to stop hadrons. Particles which are detected in the muon stations can then be identified as muons. The muon identification efficiency is about 95% while less than 2% of other particles are misidentified as muons.

3.2.4   Trigger system

At LHCb, the frequency of bunch crossings with events in the detector acceptance is around 30 MHz. Only 5 kHz of event rate could be stored, so only the physically interesting events were saved. In order to do so, a two stage trigger system was used and is introduced in the following. In Sec. 4.2 the exact trigger configurations used for this analysis are listed.

L0 The first stage are the hardware-based Level-0 triggers which aim to reduce the event rate to below 1 MHz. Possible B meson candidates preferably decay into particles with high transerverse energy (E_T) and momentum (p_T). Therefore, the two highest p_T muons and the highest E_T particle from the calorimeters are reconstructed. Only if at least one of these values pass a certain threshhold, the full detector gets read out.

High Level Trigger (HLT) The software-based HLT further reduces the rate in two steps (HLT1 and HLT2). At HLT1, only information from the VELO and the T stations is used to reconstruct first tracks and apply certain requirements on these. With this further decreased rate HLT2 can use information of all subsystems of the detector to reduce the event rate to 5 kHz which can then be recorded.

3.3   Monte Carlo simulation

Simulated events are created via Monte Carlo (MC) simulation methods. In MC simulations single events are generated via an event generator according to experimental and theoretical expectations following from the Standard Model taking the detector features into account. By so-called truthmatching, incorrectly reconstructed events can be sorted out since the true identity of every particle is known.
In this analysis, an MC sample for signal events is used to study signal distributions and their shapes.

4   Analysis strategy

In this chapter the analysis strategy for the determination of the CP asymmetry

$$A^{CP} = \frac{\mathcal{B}(B^+ \to J/\psi\, K^{*+}) - \mathcal{B}(B^- \to J/\psi\, K^{*-})}{\mathcal{B}(B^+ \to J/\psi\, K^{*+}) + \mathcal{B}(B^- \to J/\psi\, K^{*-})} \qquad (4.10)$$

with $J/\psi \to \mu^+\mu^-$ and $K^{*+} \to K^0_S \pi^+$ ($K^0_S \to \pi^+\pi^-$) is introduced, followed by an introduction to the used variables, the used data sets and the fitting procedure.

The analysis is performed in the following steps:

1. Candidate events are recorded, if they fire at least one of the trigger lines. A so-called stripping is performed on the recorded data to reduce the amount to a manageable size but keeping most of the signal events needed for the analysis (see Sec. 4.2).

2. A clean signal sample is prepared by applying additional selection cuts to the stripped data set and performing a first fit (see Sec 5.2). This signal sample is only used to train the boosted decision tree (BDT).

3. Cuts against combinatorial and peaking background are applied to the data sample created in (1) in the preselection (see Sec. 5.3).

4. In order to separate signal from background a multivariate analysis is performed by training a BDT using the signal sample created in (2) and the upper B-candidate mass sideband of the data created in (1). The input variables of the BDT do not include preselection variables. A cut on the BDT output is applied (see Sec. 5.4.).

5. A 2-D fit of the B^+ and K^{*+} masses is then performed to get the signal yield for resonant[9] decays (see Sec. 5.5).

6. In the final step, the determination of A^{CP} is performed. Here, the production and detection asymmetries are taken into account (see Sec. 6).

4.1   Variables

In particle physics one of the most commonly used variables is the four-momentum $p = (E, p_x, p_y, p_z)^T$ where E is the total energy and p_x, p_y, p_z the momentum components. It is used to deduce many other variables, e.g. the invariant mass $m = \sqrt{p^2}$. The sum of the daughters' four-momenta is the four-momentum of the mother-particle.

This section explains the most important variables used during the analysis.

---

[9]Resonant in the K^{*+} mass.

- **Transverse momentum (p_T)** describes the component of the momentum transverse to the beam axis (z-axis):

$$p_T = \sqrt{p_x^2 + p_y^2} \tag{4.11}$$

Since decay products of heavy particles such as B mesons usually have large transverse momenta, it can be used to distinguish between signal and combinatorial background.
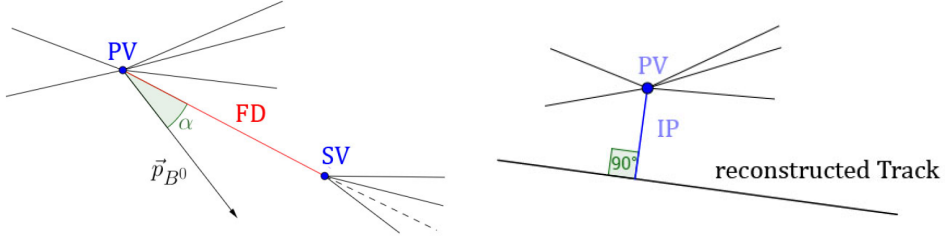
Figure 4.1: Visualisation of the used variables FD, IP and DIRA=$\cos(\alpha)$. Taken from [15].

- **Flight Distance (FD)** is the distance traveled by a particle before its decay. Thus, it is the distance between the primary vertex (PV) and the reconstructed decay vertex (see Fig. 4.1).

- **Decay Length Significance (DLS)** measures the quality of the separation of a particle's primary vertex and decay vertex. It is given by: $DLS = \frac{FD}{\sigma(FD)}$

- **Impact Parameter (IP)** is the minimal distance between the PV and the trajectory of a particle (see Fig. 4.1). It therefore describes how compatible the particle is with the hypothesis of originating from the PV. IPD-$\chi^2 = (IP/\sigma(IP))^2$ gives the significance of the value given for IP.

- **IPχ^2** of a particle measures how much the PVχ^2 changes by adding or removing its track.

- **Vertex-χ^2** is a measure for the quality of a vertex reconstruction. $\Delta\chi^2_{add-track}$ is the minimum difference of χ^2 when a new track is added to the reconstruction of a vertex. For partially reconstructed background its value should therefore be smaller than for signal.

- **DIRection Angle (DIRA)** is the cosine of the angle between the momentum vector and the vector between PV and decay vertex (see Fig. 4.1). For B mesons this angle should be very small in this analysis, resulting in DIRA$\approx$1.

- **Distance Of Closest Approach (DOCA)** measures the minimal distance of two particle trajectories.

- $DLL_{K\pi}$ **(Delta Log Likelihood)** describes how likely the hypothesis "kaon" is with respect to the default hypothesis "pion". For each particle detected the PID-system calculates a likelihood $\mathcal{L}$ for different mass hypothesis. $DLL_{K\pi}$ is then given by $\Delta log\mathcal{L}(K - \pi) = log(\mathcal{L}(K)/\mathcal{L}(\pi))$. (More information about the PID-system is given in Sec. 3.2.3).

- **Track-χ^2** is a measure for the quality of a fit of a trajectory.

- **ghostprob** gives the probability that the reconstructed track is a so-called ghost. This means that the track does not correspond to the flight path of a real particle (but is combined of measurements of several particles).

- **IsMuon** is a boolean variable and its value is set to true if the particle has measurements in at least two (three) muon stations (see Sec. 3.2.3) for low (high) momentum particles.

- **hasRich** also is a boolean variable and denotes whether or not the particle has information in the RICH system (see Sec. 3.2.3).

4.2   Dataset

Candidate	Selection requirement
B^+	$DLS > 3$
J/ψ	$2996.916\,\text{MeV} < M < 3196.946\,\text{MeV}$
	vertex$\chi^2/ndf < 20$
$\mu^\pm$	DOCA$\chi^2 < 30$
	$p_T > 500\,\text{MeV}$
	$DLL_{\mu\pi} > 0$
	isMuon= True

Table 2: Stripping cuts in `DiMuonJpsi2MuMuDetachedLine` (Stripping 21).

The data analysed in this thesis was taken with the LHCb detector in the year 2012 at a center-of-mass energy of $\sqrt{s} = 8\,\text{TeV}$ and an integrated luminosity of $2\,\text{fb}^{-1}$.

Only candidate events in which the signal B or its decay products fired the trigger are recorded. This is called triggered on signal (`TOS`). The triggers apply cuts on muon momentum, J/ψ mass, fit quality of the J/ψ decay vertex ($vertex\chi^2$), its $IP\chi^2$ and the track quality of the muons ($track\chi^2/ndf$). For a description of the trigger mechanism see Sec. 3.2.4. The choosen trigger configuration is shown in appendix A.1. The trigger lines are described in [16], [17] and [18].

To further reduce the amount of stored data to a manageable size a central selection is applied. This rough selection is called stripping. For this analysis the stripping line `DiMuonJpsi2MuMuDetachedLine` (Stripping 21, `Reco14`) is utilized, which has the requirements listed in Table 2. Events that passed the

| Candidate	Selection requirement
B^+	$4600\,\text{MeV} < M < 7000\,\text{MeV}$
	$IP\chi^2 < 16$
	$PV\chi^2_{dist} > 64$
	DIRA > 0.9995
	$\Delta\chi^2_{\text{add-track}} > 3$
	vertex$\chi^2/n_{dof} < 10$
$\mu^{\pm}$	ghostprob < 0.5
	$IPD\chi^2 > 9$
	$DLL_{\mu\pi} > 0$
	IsMuon True
K^{*+}	$p_T > 300\,\text{MeV}$
	$|M - 891.7\,\text{MeV}| < 200\,\text{MeV}$
π^+	ghostprob < 0.5
	hasRich True
	$IPD\chi^2 > 6$
	$DLL_{K\pi} < 5$
K^0_S	$|M - 497.6\,\text{MeV}| < 40\,\text{MeV}$
	vertex$\chi^2 < 25$
π_{KS}	$IPD\chi^2 > 9$

Table 3: Preselection cuts

stripping have to fulfill additional preselection cuts (see Table 3 and Fig. 4.2) as well.

A distinction is made between so-called *long tracks* and *downstream tracks*. If the K^0_S decays in the VELO (see Sec. 3.2.2), the two daughter pions leave clusters in the VELO and the T stations (and possibly in TT), so-called long tracks. For downstream tracks the mother particle decays between VELO and TT leading to signals in the TT and the T stations only. Without further selection the downstream sample contains approximately 3.3 million events and the long sample 1.6 million events. For reasons explained in Sec. 5.4, each sample is further divided into three subsamples.

4.3   Fitting procedure

To extract the unknown parameters $\vec{\lambda}$ of a given *probability density function* (PDF) f($\vec{\lambda}; \vec{x}_i$) from the data set $\vec{x}_i$ the *extended unbinned maximum likelihood*
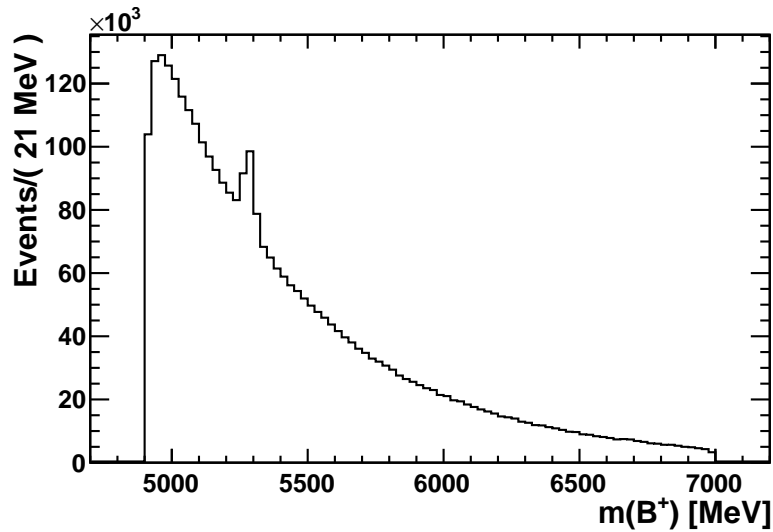
Figure 4.2: Mass spectrum of the B^+ candidate of the whole downstream sample after stripping and first preselection.

method is used for all fits in this thesis. The likelihood function for n events is defined as

$$\mathcal{L}(\vec{\lambda}) = \prod_{i=1}^{n} f(\vec{\lambda}; \vec{x_i}) \tag{4.12}$$

and expresses the probability to obtain the dataset $\vec{x_i}$ with a certain set of parameters $\vec{\lambda}$. The fitting algorithm tries to maximize the likelihood to obtain the best estimate for the parameters $\vec{\lambda}$. All fits are perfomed unbinned. For computational reasons, the negative log likelihood $-log(\mathcal{L}) = -\sum_{i=0}^{n} log f(\vec{\lambda}; \vec{x_i})$ is minimized instead. All fits are performed with the software package *ROOT* [19] and the *RooFit* [20] library. For more information about the fitting method see Ref. [21].

5 Data selection

In this section the signal selection as it was outlined in Sec. 4 is detailed. First, different background contributions are explained, followed by a description of the selection steps.

5.1 Background sources

In order to extract the number of signal events from the mass distribution, signal and background distributions have to be described accurately. Different sources of background events will be explained in this section.

5.1.1 Combinatorial background

It is possible that random particles which are not decay products of a common ancestor are selected to form a B^+. This is called combinatorial background and is the main background source in the signal region in this analysis. In the fitting of the B^+ candidate mass (see Sec. 5.2 and 5.5) an exponential function is used to describe it.

5.1.2 Partially reconstructed background

This contribution is formed by events similar to the signal channel $B^+ \to J/\psi\, K^{*+}$ where just one particle such as an π oder γ is not reconstructed or selected. The B^+ candidate mass is therefore shifted to lower values. An example is the decay $B^+ \to J/\psi\, K_1^+$ with $K_1^+ \to K^{*+}\pi^0$ where the π^0 is not reconstructed.
The proper description of this background source is one of the main challenges of the thesis.

5.1.3 Background from $B^0 \to J/\psi\, K^0$

It is possible that a random π^+ is added in the reconstruction. Then, the decay $B^0 \to J/\psi\, K^0$ with $J/\psi \to \mu\mu$ and $K^0 \to \pi^+\pi^-$ has the same final state particles as the signal channel. To exclude this contribution a cut on the invariant mass of $J/\psi\, K^0$ is applied (see Fig. 5.1).

5.1.4 Non-resonant background

The B^+ can decay directly in a J/ψ and $K_S^0\pi^+$ as well. It then has the same decay products but is featureless in the combined mass of the three pions. This fact is used to distinguish this background from signal events.

5.2 Preparation of training sample

In order to train an effective BDT (see Sec. 5.4) a clean signal template is needed. Therefore hard cuts (see Table 4) are applied to the stripped data to get rid of background events but still keep enough signal events.

A fit of the mass of the B^+ candidate is then performed. An exponential function is used to describe the combinatorial background, a hybrid of an exponential and a Gaussian called ExpAndGauss for the shoulder of partially reconstructed events and two Crystal Ball (CB) shapes with common mean and sigma for the signal contribution.

ExpAndGauss is given by:

$$f(x|\mu, t, \sigma) = \begin{cases} C \cdot exp(\beta x) & x \le t \\ exp\left(-0.5 \cdot \left(\frac{x-\mu}{\sigma}\right)^2\right) & x > t \end{cases} \tag{5.13}$$
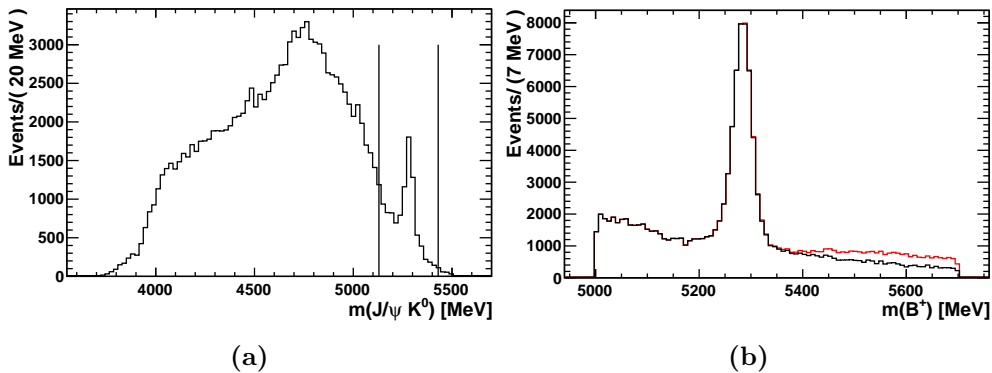
with

$$C = exp\left(-0.5 \cdot \left(\frac{t-\mu}{\sigma}\right)^2\right) \cdot exp(-\beta \cdot t) \tag{5.14}$$

$$\beta = \frac{\mu - t}{\sigma^2} \tag{5.15}$$

and the parameters μ, t and σ.

The Crystall Ball function is an empirical shape named after the Crystal Ball collaboration to describe the asymmetric shape of mass distributions with energy

Figure 5.1: The invariant mass of $J/\psi K^0$ is shown (a). The two vertical lines indicate the region excluded for the analysis. Additionally, the mass spectrum of the B^+ candidate is shown (b), in red after the preselection cuts given in Table 5 without the cut on $m(J/\psi K^0)$ and in black including this cut. Both figures show the data of the whole downstream sample.

loss involved (see [22]). It is a Gaussian with a power law tail on one side. The shape is given by:

$$f(x|\alpha, n, \mu, \sigma) = N \cdot \begin{cases} exp\left(-\frac{(x-\mu)^2}{2\sigma^2}\right) & \frac{x-\mu}{\sigma} > -\alpha \\ A \cdot \left(B - \frac{x-\mu}{\sigma}\right)^{-n} & \frac{x-\mu}{\sigma} \leq -\alpha \end{cases} \qquad (5.16)$$

with

$$A = \left(\frac{n}{|\alpha|}\right)^n \cdot exp\left(-\frac{|\alpha|^2}{2}\right) \qquad (5.17)$$

$$B = \frac{n}{|\alpha|} - |\alpha| \qquad (5.18)$$

$$N = \frac{1}{\sigma(C + D)} \qquad (5.19)$$

$$C = \frac{n}{|\alpha|} \cdot \frac{1}{n-1} \cdot exp\left(-\frac{|\alpha|^2}{2}\right) \qquad (5.20)$$

$$D = \sqrt{\frac{\pi}{2}}\left(1 + erf\left(\frac{|\alpha|}{\sqrt{2}}\right)\right) \qquad (5.21)$$

where μ and σ are mean and width of the Gaussian, α gives the threshold of the power law tail and n its shape.
The complete fit model is then given by:

$$\mathcal{P}_{full} = N_{sig}\mathcal{P}_{sig} + N_{cbg}\mathcal{P}_{cbg} + N_{part}\mathcal{P}_{part} \qquad (5.22)$$
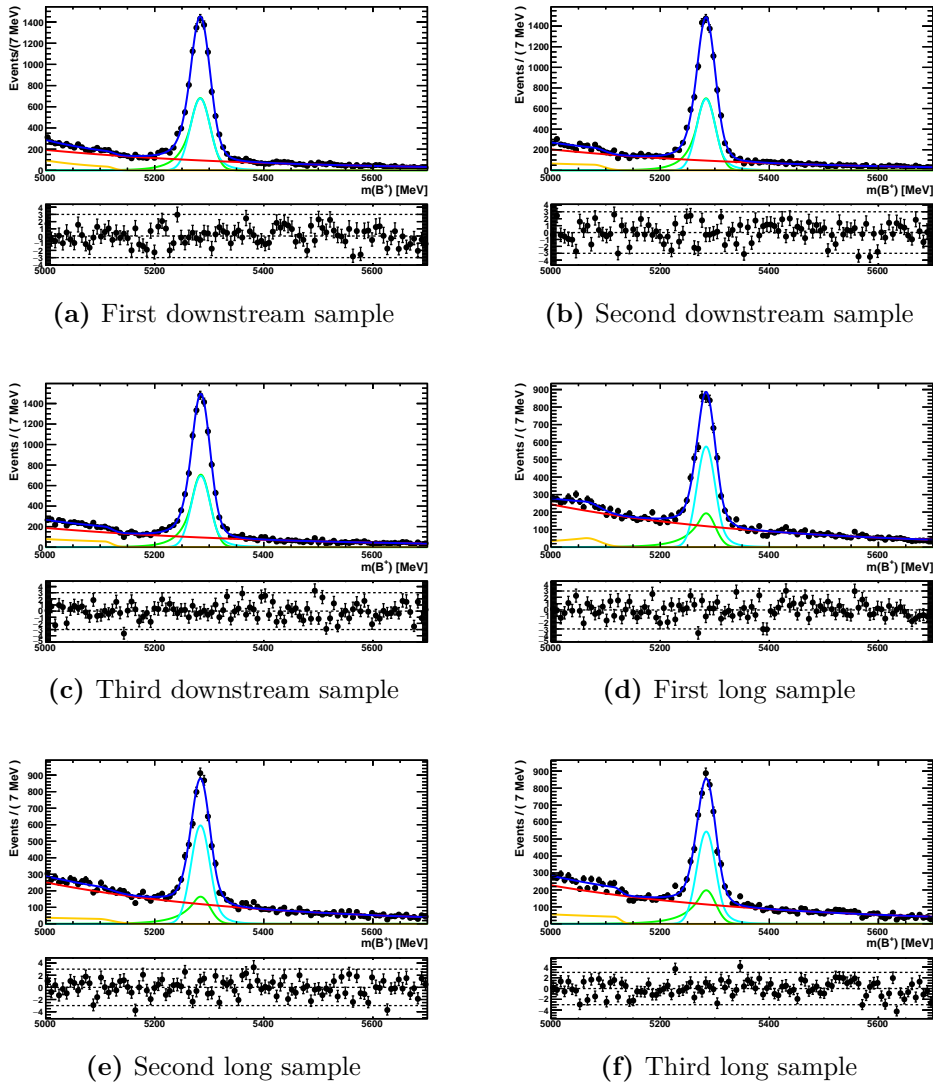
$$\mathcal{P}_{sig} = f \cdot CB(x|\alpha_1, n_1, \mu, \sigma_1) + (1 - f) \cdot CB(x|\alpha_2, n_2, \mu_1, \sigma_1) \qquad (5.23)$$

In Sec. 5.4 clean signal contributions of the BDT input variables are needed. Since signal and background can be distinguished in the B^+ mass, the result of this fit (see Fig. 5.2) is used to calculate so-called *sWeights* for every event. Applying these sWeights on the data sample results in background subtracted signal distributions. A detailed explanation of the $_s\mathcal{P}lot$ technique is given in [23].
The upper B candidate mass sideband ($m_{B+} > 5700\,\text{MeV}$) of the stripped data is used as a (combinatorial) background template.

Candidate	Selection requirement
B^+	DIRA > 0.99995
	vertex$\chi^2/ndf < 5$
π^+	$DLL_{K\pi} < 0$
$\pi_{K_S^0}$	$DLL_{K\pi} < 5$
K_S^0	$p_T > 800\,\text{MeV}$
	$|m(J/\psi\,K^0) - 5280\,\text{MeV}| > 150\,\text{MeV}$

Table 4: Cut for preparation of signal sample

(a) First downstream sample

(b) Second downstream sample

(c) Third downstream sample

(d) First long sample



(e) Second long sample

(f) Third long sample

Figure 5.2: Fit results of all six subsamples. Blue shows the total fit, red the combinatorial background, yellow the partially reconstructed background and turquoise and green the two CB for signal.

5.3   Preselection

A preselection with looser cuts was applied (see Table 5). These cuts together with the later trained BDT (see Sec. 5.4) are more efficient than the harder cuts in means of excluding less signal events and therefore leading to better statistics.

Candidate	Selection requirement
B^+	DIRA > 0.9999
	vertex$\chi^2/ndf < 5$
π^+	$PIDK < 5$
K_S^0	$p_T > 800\,\text{MeV}$
	$|m(J/\psi\,K^0) - 5280\,\text{MeV}| > 150\,\text{MeV}$

Table 5: Preselection cuts
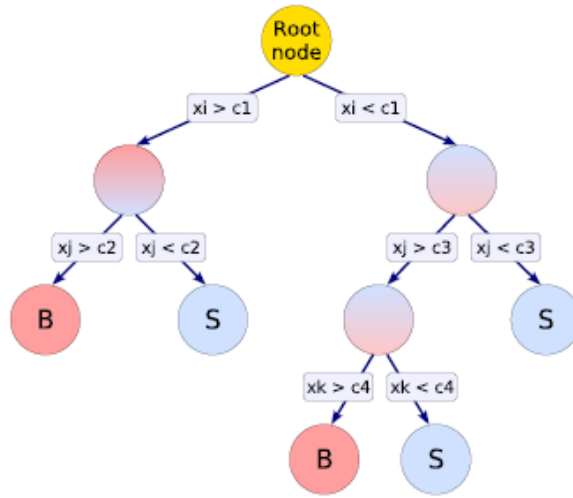
Figure 5.3: Scheme of a single decision tree. At each node a one-dimensional cut c_i in the input-variable x_i is performed which optimally discriminates signal from background. Leaf nodes are labelled S for signal or B for background depending the majority of its entries. Taken from [24].

5.4   Multivariate analysis

So far, only linear and separate cuts on different variables are applied. If the variables are not independent of each other, more complicated non-linear cuts would be more efficient. In order to perform the best combination of these non-linear cuts the Toolkit for Multivariate Data Analysis with Root (TMVA [24]) is used. TMVA provides a lot of different methods and algorithms suited for a wide range of different analyses. In this thesis a *Bosted Decision Tree* (BDT) is applied (see [25]). The BDT takes several input variables and calculates the signal-likeliness of an event which can be used to discriminate signal and background. First, the BDT has to be trained. Therefore signal and background templates have to be provided. A single decision tree consists of several nodes where at each node the events are sorted by a binary cut (see Fig. 5.3). After

running through all the nodes every event ends up in a so-called leaf. Depending on the leaf the events gets classified as signal- or background-like. The variable and cut for each node are determined by minimizing the so-called Gini-impurity $p(p-1)$ where p is the fraction of signal in the node. It has its minimal value for a sample containing pure signal or background events and is maximal for 50% signal. This algorithm will be repeated till a stopping criterion is fulfilled. To not have an overtraining effect[10], pruning is used as stopping criterion in most cases.

To make up for the pruning and increase the separation power, boosting is used where instead of a single tree a whole forest of trees is trained. Events that are misclassified in one tree will get a higher weight for the next tree to make the whole process more sensitive to those events. Each event gets then classified by the BDT-output which is a weighted sum of all tree responses. The higher the BDT response of an event the more background like it is.

In this thesis the AdaBoost-algorithm was used (see [24]). The used sWeighted

Candidate	used variable
B^+	FD
	$IP\chi^2$
	p_T
K^{*+}	p_T
μ	$\max(IP\chi^2)$

Table 6: Input variables of the BDT. In Sec. 4.1 all used quantities are introduced.

signal sample and the background sample are described in Sec. 5.2. A list of the input parameters for the trained BDT can be found in Table 6 and their distributions are shown in Fig. 5.4. It is important that these input variables do not include the ones used in the preselection.

As described in Sec. 4.2 the events are separated in a long track and a downstream sample. Both samples are further divided randomly in three subsamples. A BDT is then trained with one of the subsamples, a second subsample is used to obtain the optimal cut value for the BDT which is then applied to the third subsample. This is done in cyclical permutations for all subsamples. The optimal cut value is obtained by maximizing the figure of merit $\frac{S}{\sqrt{S+B}}$ where S and B are the number of signal and background events, respectively. This is done by estimating the number of signal and background events in the signal region with a fit. The BDT output and figure of merit for one of the downstream subsamples is shown in Fig. 5.5. The resulting optimal BDT cuts are given in Table 7.

---

[10]A tree can become sensitive to statistical fluctuations of a data sample. It then performs perfect for the training sample but worse on a testing sample. To check possible overtraining effect the BDT-output of a similar test sample can be compared with the training sample.

|	sample 1	sample 2	sample 3
long	-0.0655	-0.0542	-0.0585
downstream	-0.1103	-0.1143	-0.1114

Table 7: Optimal cuts for the BDT output for all six data samples. The differences are small as it is expected.

5.5   2-D fit

As explained in Sec. 5.1.4, one can distinguish signal and non-resonant background by the mass distribution of the K^{*+} candidate. To determine the number of signal events a 2-D fit on the masses of the B^+ and K^{*+} is performed. In order to reduce the number of fit parameters only events with B^+ masses larger than 5200 MeV are taken into account, thus excluding the partially reconstructed background. A systematic uncertainty is assigned to take into account the effect of this requirement (see Sec. 7).

For the B^+ mass the same shapes as described in Sec. 5.2 are used. The non-resonant background is fitted by the same double CB as the signal. For the signal peak in the K^{*+} mass a Breit-Wigner shape given by

$$f(m_{K^{*+}}|\mu, \Gamma) = \frac{1}{2\pi} \frac{\Gamma}{(m_{K^{*+}} - \mu)^2 + \Gamma^2/4} \tag{5.24}$$
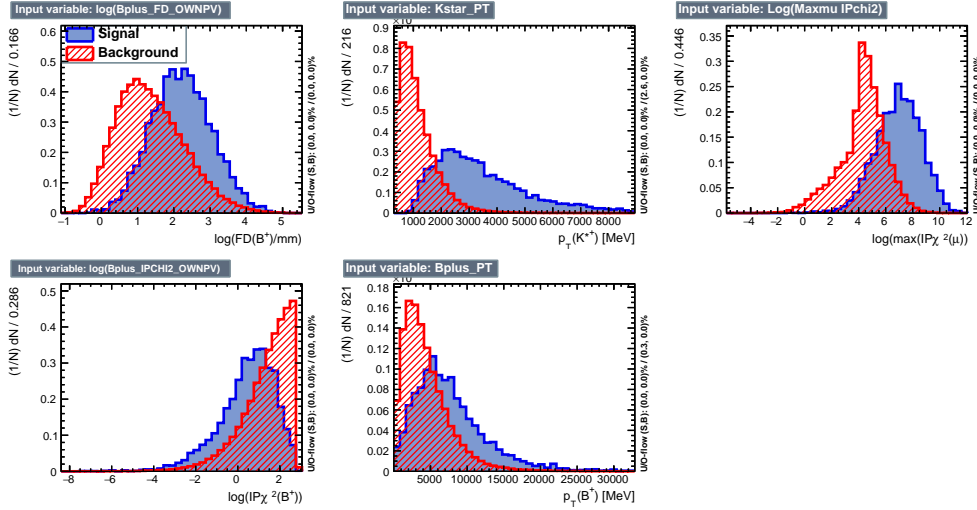
Figure 5.4: Input variables of the trained BDT. Blue denotes signal and red background. The first downstream sample is shown.
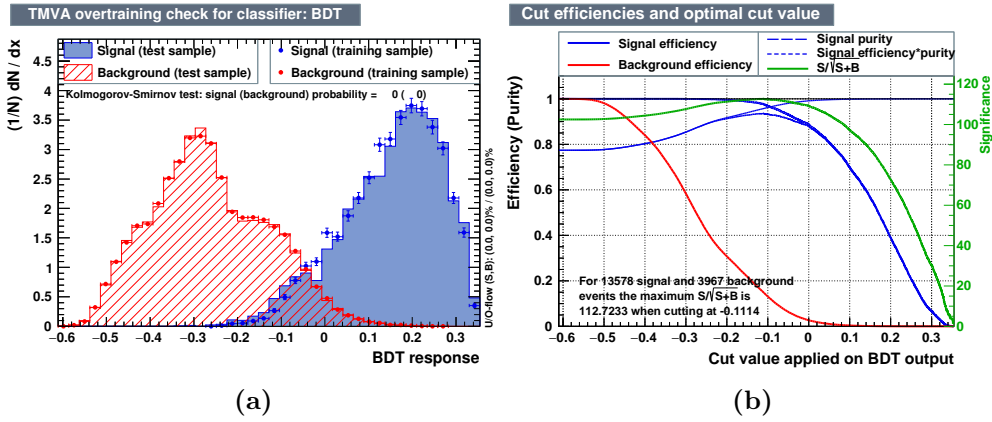
Figure 5.5: (a) BDT response for training and testing sample. The training sample is displayed as dots, the testing sample as filled areas. Both have similar distributions which is consistent with no overtraining. Results for the same downstream sample is shown as before. (b) Cut efficiencies are shown. The optimal cut value to maximize the figure of merit $\frac{S}{\sqrt{S+B}}$ for 13578 signal and 3967 background events is -0.1114. Signal and background yield are obtained by a fit on the first downstream sample. The BDT and its cut are then applied on the third sample.

with the mean μ and width Γ is used. For the combinatorial background the following two body phase space approximation is used:

$$f(m_{K^{*+}}|m_{thresh}, c) = (m_{K^{*+}} - m_{thresh})^c \quad (5.25)$$

where m_{thresh} is the sum of the π and K_S^0 masses and c a free parameter. Non-resonant decays are fitted with a first order polynomial. The full fit model is then described by:

$$\mathcal{P}_{full}(m_{B^+}, m_{K^{*+}}) = N_{sig}\mathcal{P}_{2CB}(m_{B^+})\mathcal{P}_{BW}(m_{K^{*+}}) \quad (5.26)$$
$$+N_{cbg}\mathcal{P}_{exp}(m_{B^+})\mathcal{P}_{2bps}(m_{K^{*+}}) \quad (5.27)$$
$$+N_{nonres}\mathcal{P}_{2CB}(m_{B^+})P_{poly}(m_{K^{*+}}) \quad (5.28)$$

Here, the decay $B^+ \to J/\psi K^{*+}$ and the charged conjugate process are treated separately. The fits for both processes are performed simultaneously with common parameters for the distributions and the same fraction $frac = \frac{N_{sig}}{N_{nonres}}$. The fit results are shown in Fig. 5.6 and the signal yields in Table 8.
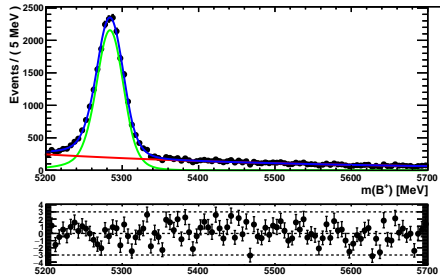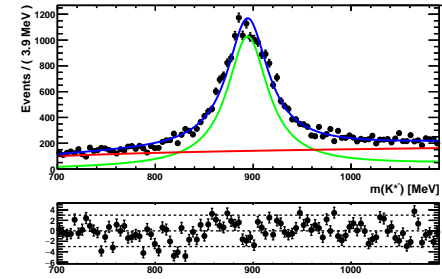
(a) Mass spectrum of the B^+ candidate in the downstream sample.
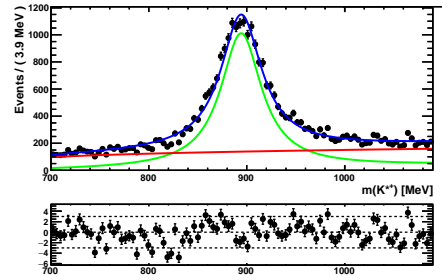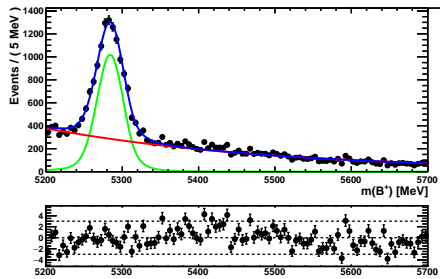
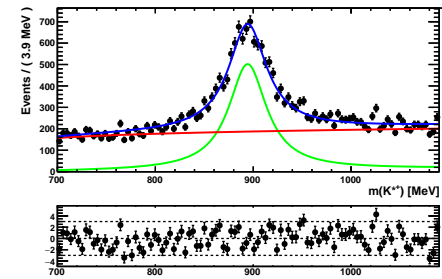(b) Mass spectrum of the K^{*+} candidate in the downstream sample.
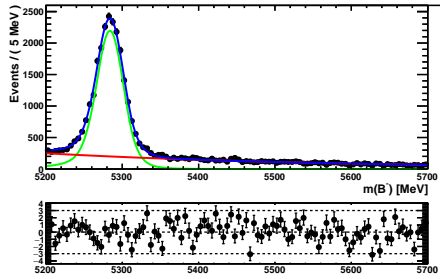
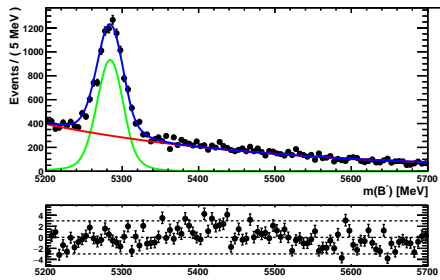(c) Mass spectrum of the B^- candidate in the downstream sample.

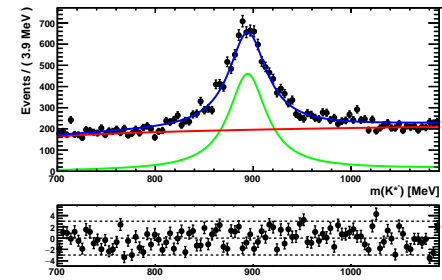(d) Mass spectrum of the K^{*-} candidate in the downstream sample.

(e) Mass spectrum of the B^+ candidate in the long sample.

(f) Mass spectrum of the K^{*+} candidate in the long sample.

(g) Mass spectrum of the B^- candidate in the long sample.

(h) Mass spectrum of the K^{*-} candidate in the long sample.

Figure 5.6: Fit results for the 2-D fit for all samples of the decay $B^+ \rightarrow J/\psi K^{*+}$ (and the charge conjugate process). Green indicates signal and non-resonant background, red the combinatorial background and blue the total fit model.

6   Determination of the CP asymmetry

This chapter gives a detailed description of how the CP asymmetry

$$A^{CP} = A^{CP}_{raw} - A_{Kaon} - A_{prod} \tag{6.29}$$

is determined where A^{CP}_{raw} is the raw asymmetry measured, A_{prod} the production asymmetry of B^+ and B^- and A_{Kaon} the asymmetry induced by the neutral Kaons. Equ. 6.29 is an approximation and valid for small asymmetries.

6.1   Raw *CP* asymmetry

The 2-D fits introduced in Sec. 5.5 lead to the numbers given in Table 8. The raw CP asymmetry can then be calculated via

$$A^{CP}_{raw} = \frac{N(B^- \to J/\psi\, K^{*-}) - N(B^+ \to J/\psi\, K^{*+})}{N(B^- \to J/\psi\, K^{*-}) + N(B^+ \to J/\psi\, K^{*+})} \tag{6.30}$$

leading to $A^{CP}_{raw,L} = (-4.38 \pm 1.17)\%$ for the long track sample and $A^{CP}_{raw,D} = (+0.87 \pm 0.69)\%$ for the downstream track sample. The statistical error is given by

$$\sigma(A^{CP}_{raw}) = \sqrt{\left(\frac{2N(B^+)\sigma(N(B^-))}{(N(B^+) + N(B^-))^2}\right)^2 + \left(\frac{2N(B^-)\sigma(N(B^+))}{(N(B^+) + N(B^-))^2}\right)^2} \tag{6.31}$$

6.2   Production asymmetry

The measured raw CP asymmetry has to be corrected by possible asymmetries in the production of B^+ and B^- at LHCb:

$$A_{prod} = \frac{N(B^-) - N(B^+)}{N(B^-) + N(B^+)} \tag{6.32}$$

where $N(B^-)$ and $N(B^+)$ denote the number of B^- and B^+ produced, respectively. This production asymmetry integrated over transverse momenta in the range $2 < p_T < 30\ GeV$ has been measured to be

$$A_{prod}(B^+\sqrt{s} = 8\,\text{TeV}) = (-0.53 \pm 0.33)\% \tag{6.33}$$

by the LHCb collaboration [26]. It is the same for long and downstream tracks.

	long	downstream
$N(B^+ \to J/\psi\, K^{*+})$	8658 ± 141	18569 ± 182
$N(B^- \to J/\psi\, K^{*-})$	7932 ± 133	18895 ± 184

Table 8: Number of signal events of the different samples. The errors denote the uncertainty of the 2-D fit.
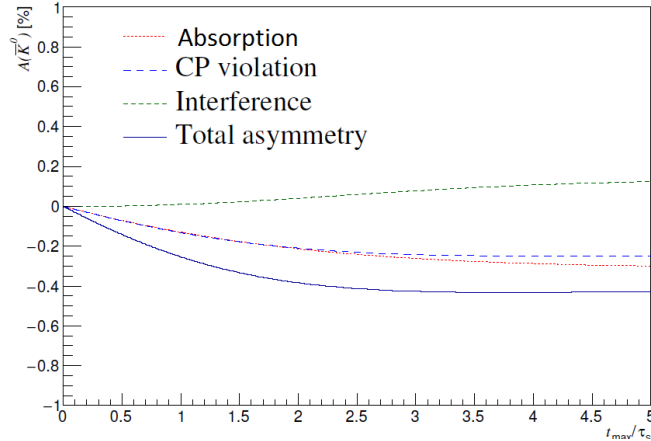
Figure 6.1: Time integrated neutral kaon asymmetry for an average K_S^0 momentum of 23.7 GeV. $t_{max}/\tau_S \approx 0.5$ for long tracks and $t_{max}/\tau_S \approx 2$ for downstream tracks. The underlying model assumes a constant material distribution (for more information, see [27]).

6.3   Neutral kaon asymmetry

The flavor of the neutral kaon in this analysis is given by $K^{*+} \to K^0 \pi^+$ and $K^{*-} \to \overline{K}^0 \pi^-$ in the decay of B^+ and B^-, respectively. However, the mass eigenstates of the neutral kaon system are K_S^0 and K_L^0 and thus inducing a mixing of K^0 and $\overline{K}^0$. Here, neutral kaons are reconstructed in the CP eigenstate $\pi^+\pi^-$. Since K_S^0 and K_L^0 are not CP eigenstates, the decay $K_S^0 \to \pi^+\pi^-$ is CP violating. Also the different absorption rates of K^0 and $\overline{K}^0$ in the detector have to be taken into account.

The effects of mixing, CP violation, absorption and their interference have been simulated by a simplified detector model, provided by [27]. With the average K_S^0 momentum of 23.7 GeV and the maximal FD of the kaons the asymmetry A_{Kaon} can be deduced for both long and downstream tracks. Fig. 6.1 shows the time integrated asymmetry for this simplified model. The deduced asymmetries from neutral kaons are $A_{Kaon,L} \approx -0.15\%$ for long and $A_{Kaon,D} \approx -0.40\%$ for downstream tracks.

6.4   *CP* asymmetry

With Equ. 6.26 the CP asymmetry of the decay $B^+ \to J/\psi\, K^{*+}$ is determined to $A_L^{CP} = (-3.70 \pm 1.17)\%$ and $A_D^{CP} = (+1.80 \pm 0.69)\%$ for long and downstream tracks, respectively. The weighted average is given by

$$A_{tot}^{CP} = \frac{w_L A_L + w_D A_D}{w_L + w_D} \tag{6.34}$$

where the weights w_i are given by $w_i = \frac{1}{\sigma_i^2}$ with statistical uncertainties σ_i.
The total CP asymmetry is then $A^{CP} = (+0.40 \pm 0.60)\%$. Only the statistical uncertainty given by the fit results is shown here. The determination of other, systematic uncertainties is done in the next section.
Potential asymmetries in the detection of charged pions are thought to be negligible since approximately the same amount of magnet up and magnet down data is used.

7 Systematic uncertainties

This section gives a brief overview about systematic uncertainties of the CP asymmetry measurement. As the realization of this thesis was limited in time only a few uncertainties could be studied. They are thought to contribute the most. At the end of this chapter, a short outlook on other possible uncertainties is given. The quantified systematic uncertainties are the following:

- **Partially reconstructed background:** One of the main sources of uncertainties is the fit range. As discussed in Sec. 5.5, only events with a reconstructed B^+ mass larger than 5200 MeV are taken into account, therefore trying to exclude partially reconstructed background which is shifted to lower masses. The effect of this cut is studied by performing a 1-D fit on the B^+ mass for the range [5000,5700] MeV with partially reconstructed background and the range [5200,5700] MeV without a partially reconstructed background contribution. The difference of the determined yields and thereby deduced asymmetries is calculated to be $\sigma(A_{raw,part,L}^{CP}) = 0.76\%$ and $\sigma(A_{raw,part,D}^{CP}) = 0.37\%$ for long tracks and downstream tracks, respectively. It is taken as the first systematic uncertainty.

- **Fit ranges:** Another systematic uncertainty is due to the chosen fit ranges of the B^+ and K^{*+} masses. It is determined by performing fits on different mass windows. First, the range of the B^+ is changed while the range for K^{*+} is kept constant at [700,1090] MeV. Used B^+ mass ranges are: [5200,5600] and [5200,5500] MeV. Then, the range for the K^{*+} is changed to [750,1050] MeV while B^+ is fitted in the usual [5200,5700] MeV range. The last fit leads to the largest difference and is thus taken as the uncertainty induced by the fit ranges as $\sigma(A_{raw,range,L}^{CP}) = 0.40\%$ and $\sigma(A_{raw,range,D}^{CP}) = 0.10\%$ for long and downstream tracks, respectively.

- **Model for combinatorial background:** The shape for the combinatorial background in the reconstructed K^{*+} mass is changed from the two body phase space approximation described in Sec. 5.5 to a second order polynomial. The determined difference is taken as uncertainty: $\sigma(A_{raw,comb,L}^{CP}) = 0.05\%$ and $\sigma(A_{raw,comb,D}^{CP}) = 0.01\%$ for the long track and the downstream track sample, respectively.

- **Fraction of non-resonant decays:** As described in Sec. 5.5 the fraction of non-resonant decays is fitted as an common parameter in the decays of B^+ and B^-. This introduces an uncertainty which is determined by fixing this fraction for the long track sample to the value determined in the downstream sample and vice versa. The difference to the determined asymmetry is taken as uncertainty and is $\sigma(A_{raw,frac,L}^{CP}) = 0.02\%$ and $\sigma(A_{raw,frac,D}^{CP}) = 0.01\%$ for long and downstream tracks, respectively.

- **Production asymmetry:** As mentioned in Sec. 6.2, the production asymmetry of the B^+ meson has a uncertainty of $\sigma(A_{prod}) = 0.33\%$ for both samples.

- **Neutral kaon:** The uncertainty due to the neutral kaon asymmetry is estimated to be $\sigma(A_{Kaon}) = 0.20\%$ for both samples.
  A summary of all contributions can be found in Table 9. By calculating the quadratic sum of all described contributions and and using error propagation, the total systematic is determined to be $\sigma(A_{syst.}^{CP}) = 0.48\%$. Other possible sources for uncertainties are a possible detection asymmetry of π^+ and π^- which indicate the flavor of the initial particle (B^+ or B^-, respectively). The effect of this asymmetry is thought to be negligible but has to be studied further. Additionally, the used Breit-Wigner shape for the signal in the K^{*+} mass is not completely correct. For particles of low mass the width depends on the mass and a relativistic Breit-Wigner has to be used for a completely correct description.
  It should be noted that the total systematic uncertainty in this analysis is smaller than the statistical uncertainty.

Source	Absolute uncertainty[%]	
	Long track	downstream track
Partially reconstructed background	0.76	0.37
Fit range	0.40	0.16
Model for combinatorial bgd	0.05	0.01
Fraction of non-resonant decay	0.02	0.01
Production asymmetry	0.33	0.33
Neutral kaons	0.20	0.20
Quadratic sum	0.94	0.56

Table 9: Summary of all contributions to the systematic uncertainty.

8 Summary and outlook

A measurement of the CP asymmetry in the decay $B^+ \to J/\psi\, K^{*+}$ is presented in this thesis, where the J/ψ decays into two muons and K^{*+} is reconstructed as $K^0_S \pi^+$ with $K^0_S \to \pi^+ \pi^-$. The data was taken in the year 2012 in Run I of the LHCb experiment.

To reduce the amount of combinatorial background preselection cuts are applied and a Boosted Decision Tree is used. For its training a clean signal sample is needed which is obtained via the $_s\mathcal{P}lot$ technique. In the preselection an additional cut is applied to reduce background from the decay $B^0 \to J/\psi\, K^0$ and partially reconstructed processes. Afterwards, a final 2-D fit is performed to the B^+ and K^{*+} candidates' masses to determine the number of signal events. This results in a CP asymmetry of

$$A^{CP}(B^+ \to J/\psi\, K^{*+}) = (+0.40 \pm 0.60(\text{stat.}) \pm 0.48(\text{syst.}))\%.$$

which agrees with the value of $A^{CP} = (-4.8 \pm 2.9(\text{stat.}) \pm 1.6(\text{syst.}))\%$ measured by the BABAR collaboration [3] but has smaller statistical and systematic uncertainties.

The measurement performed in this thesis is dominated by statistical uncertainties. To decrease the statistical uncertainty more data is needed, e.g. from Run II of the LHC which started in 2015. Also the trained BDT could be optimized to get a better figure of merit. To reduce the systematic effects the partially reconstructed background has to be studied further, e.g. by training another BDT specialized on this background source. Additional MC samples for the individual contributions can help to increase the accuracy of the fit, but also to find possible background and signal discriminating variables. Additionally, a more detailed model for the CP asymmetry caused by neutral kaons could be implemented.

A   Appendix

A.1   Trigger configuration

Stage	Triggers
L0	`L0MuonDecision`
HLT1	`Hlt1TrackAllL0Decision` or `Hlt1TrackMuonDecision` or `Hlt1DiMuonHighMassDecision`
HLT2	`Hlt2TopoMu2BodyBBDTDecision` or `Hlt2DiMuonDetachedJpsiDecision`

Table 10: Chosen trigger configuration for candidate events.

References

[1] M. Thomson, *Modern particle physics*, Cambridge University Press, 2013.

[2] G. Aad *et al.*, *Observation of a new particle in the search for the Standard Model Higgs boson with the ATLAS detector at the LHC*, Physics Letters B **716** (2012).

[3] B. Aubert *et al.*, *Measurement of branching fractions and charge asymmetries for exclusive B decays to charmonium*, Physical review letters **94** (2005).

[4] Dsperlich, *Standard Model of Elementary Particles*, `https://commons.wikimedia.org/wiki/File:Standard_Model_of_Elementary_Particles.svg`. [visited on 13/02/2017].

[5] R. Aaij *et al.*, *Observation of J/ψ p Resonances Consistent with Pentaquark States in $\Lambda_b^0 \to J/\psi K^- p$ decays*, Physical review letters **115** (2015).

[6] M. Peskin and D. Schroeder, *Quantum field theory*, Westview Press, 1995.

[7] LHCb collaboration, A. A. Alves Jr. *et al.*, *The LHCb detector at the LHC*, JINST **3** (2008) S08005.

[8] CERN, *LHCb experiment*, `https://lhcb-public.web.cern.ch/lhcb-public/en/detector/Detector-en.html`. [visited on 16/02/2017].

[9] G. Aad *et al.*, *The ATLAS experiment at the CERN Large Hadron Collider*, JINST **3** (2008) S08003.

[10] S. Chatrchyan *et al.*, *The CMS experiment at the CERN LHC*, JINST **3** (2008) S08004.

[11] K. Aamodt *et al.*, *The ALICE experiment at the CERN LHC*, JINST **3** (2008) S08002.

[12] L. Collaboration, *LHCb detector performance*, International Journal of Modern Physics A (2015).

[13] LHCb Collaboration, *LHCb Silicon Tracker*, `http://lhcb.physik.uzh.ch/ST/public/material/index.php`. [visited on 26/02/2017].

[14] M. o. Adinolfi, *Performance of the LHCb RICH detector at the LHC*, The European Physical Journal C **73** (2013).

[15] D. Baitinger, *Measurement of the branching ratio of the decay $B^+ \to J/\psi K^{*+}$ at the LHCb experiment* , Bachelor thesis. University of Heidelberg (2016).

[16] R. Aaij and J. Albrecht, *Muon triggers in the high level trigger of LHCb*, tech. rep., 2011.

[17] V. Gligorov *et al.*, *The HLT inclusive B triggers*, tech. rep., 2011.

[18] M. Williams *et al.*, *The HLT2 topological lines*, tech. rep., 2011.

[19] R. Brun and F. Rademakers, *ROOT-an object oriented data analysis framework*, Nuclear Instruments and Methods in Physics Research (1997).

[20] W. Verkerke, D. Kirkby *et al.*, *The RooFit toolkit for data modeling*, Statistical Problems in Particle Physics, Astrophysics and Cosmology (2003).

[21] C. Croarkin and W. Guthrie, *NIST/SEMATECH e-Handbook of Statistical Methods*, Available at:/http://www. itl. nist. gov/div898/handbook/S (2015).

[22] T. Skwarnicki, *A study of the radiative cascade transitions between the Upsilon-prime and Upsilon resonances*, tech. rep., DESY, 1986.

[23] M. Pivk and F. R. Le Diberder, *A statistical tool to unfold data distributions*, Nuclear Instruments and Methods in Physics Research Section **555** (2005).

[24] A. Hoecker *et al.*, *TMVA-Toolkit for multivariate data analysis*, arXiv preprint physics/0703039 (2007).

[25] I. Narsky and F. C. Porter, *Statistical analysis techniques in particle physics*, John Wiley & Sons, 2013.

[26] R. Aaij *et al.*, *Measurement of the $B^{\pm}$ production asymmetry and the CP asymmetry in $B^{\pm} \to J/\psi K^{\pm}$ decays*, arXiv preprint arXiv:1701. 05501 (2017).

[27] S. Stahl, *Measurement of CP asymmetry in muon-tagged $D^0 \to K^- K^+$ and $D^0 \to \pi^- \pi^+$ decays at LHCb*, Dissertation. University of Heidelberg (2014).

Acknowledgements

Erklärung

Ich versichere, dass ich diese Arbeit selbstständig verfasst und keine anderen als die angegebenen Quellen und Hilfsmittel benutzt habe

Heidelberg, den 13.03.2017

Christoph Rieß